electronic materials

MDPI

Article

Synthesis and Characterization of Aero-Eutectic Graphite Obtained by Solidification and Its Application in Energy Storage: Cathodes for Lithium Oxygen Batteries

Ricardo Walter Gregorutti [1,*], Alvaro Yamil Tesio [2], Juan Luis Gómez-Cámer [3] and Alicia Norma Roviglione [4]

[1] Laboratorio de Entrenamiento Multidisciplinario para la Investigación Tecnológica—CICPBA, Av. 52 e/121 y 122, La Plata B1900AYB, Argentina

[2] Centro de Investigación y Desarrollo en Materiales Avanzados y Almacenamiento de Energía de Jujuy (CIDMEJu), Centro de Desarrollo Tecnológico General Manuel Savio, Av. Martijena W/N, Palpalá Y4612, Argentina; atesio@cidmeju.unju.edu.ar

[3] Departamento de Química Inorgánica, Instituto Universitario de Investigación en Química Fina y Nanoquímica (IUNAN), Campus de Rabanales, Universidad de Córdoba, 14071 Córdoba, Spain; jl.gomez@uco.es

[4] Departamento de Ingeniería Mecánica, Facultad de Ingeniería, Universidad de Buenos Aires, Av. Paseo Colón 850, Ciudad Autónoma de Buenos Aires C1063ACV, Argentina; arovi@fi.uba.ar

* Correspondence: ricardo.gregorutti@cyt.cic.gba.gob.ar; Tel.: +54-0221-483-1141

Received: 29 July 2020; Accepted: 30 August 2020; Published: 3 September 2020

Abstract: Aero-eutectic graphite can be defined as a new light material with hierarchically structured porosity. It is obtained from the solidification of gray cast irons, followed by the dissolution of the ferrous matrix by an acidic sequence. The result is a continuous and interconnected network of graphite sheets with varied dimensions randomly oriented. X-ray diffraction characterization has revealed graphite crystallographic planes (002), (100), (101), (102) and (004), while the surface area measured by BET and Langmuir methods has been determined in the order of 90 m^2 g^{-1} and 336 m^2 g^{-1}, respectively. The process of obtaining eutectic aero-graphite also allows the deposit of Cu nanofilms and TiC particles. Aero-eutectic graphite has been tested as cathode in Li–O_2 batteries as it has been prepared, without the addition of binders or conductive carbons, showing an appropriate contact with the electrolyte, so that the oxygen reduction and evolution reactions may develop satisfactorily. In the discharge-charge galvanostatic tests, the battery accomplishes 20 complete cycles with area capacity limited to 1.2 mAh cm^{-2}.

Keywords: porous graphite; hierarchical porous structure; Li–O_2 battery cathode

1. Introduction

The limited reserves of fossil fuels and the adverse effects that they may generate on the environment have led to the development of renewable energies, among which solar and wind power stand out. The great potential of these energy sources can only be exploited efficiently if reliable and secure electrical energy storage devices (EES) are provided. Many of the EES are batteries, fuel cells, flow batteries and electrochemical capacitors, which have carbon in some of their components, such as electrodes.

A side effect of the use of fossil fuels such as coal and oil is the emanation of CO_2, which has contributed significantly to global warming during the last century due to the greenhouse effect it generates [1–3].The separation of CO_2 requires new porous materials that act as absorbents of this

compound to reduce environmental pollution. For this purpose, it is necessary that the absorbent has a specific surface area, appropriate pore size and an interconnection that facilitates gas diffusion. Again, porous carbons with appropriate specific functionality are an important alternative to act as an absorber for toxic gases such as CO_2 [4].

Why is carbon one of the most used materials for those applications? One of the most important properties is its high electrical conductivity that is highly restricted to the absence of defects in the crystalline structure. Other feature is its chemical stability that explains its wide insolubility in most solvents used in Li–O_2 batteries as dimethyl sulfoxide, acetonitrile, dimethoxyethane and tetraethylene glycol dimethyl ether [5]. While not all carbons present these characteristics, pure 100% crystalline graphite is the variety that manages to meet both.

As it has been previously mentioned, a high specific surface area, certain pore shapes and sizes, and access paths that facilitate ion transport are required to achieve a higher performance. Functionally assembled porous structures, in which the pores have tortuosity factors, different shapes and aspect ratios, with sizes varying from nanometres to millimetre scales are known as hierarchically structured porous materials (HSPM) [6–11]. The development of HSPM has been complex and with high manufacturing costs [12–14].

The challenge is to find a simple way to obtain HSPM, and at the same time, avoiding complex processes, such as polymerization, sintering, pyrolysis, use of templates or mixing with other expensive commercial materials. To this end, the present work proposes an HSPM graphite obtained from gray cast iron, which is a low-cost material, widely used in the metal-mechanical industry.

Gray cast irons are based on Fe–C–Si alloys, which solidify as an irregular stable eutectic characterized by excellent physical properties and low production costs, whose chemical composition is about 2–4 wt.% of carbon, 1.8–2.7% of silicon and balance of iron. Carbon is mostly present as pure graphite, distributed in a network of interconnected sheets, in the ferrous matrix [15,16]. Graphite is one of the allotropic varieties of carbon (sp^2) characterized by a mostly hexagonal crystalline structure (D6h4-PG3/mmc), with a smaller proportion of rhombohedral graphite (D3d5-R3m) [17].

By modifying solidification parameters different morphologies and distributions of laminar graphite are obtained, classified by ASTM A247 standard [18]. According to the aforementioned classification, different hierarchical graphite structures could be obtained by means of having large interfacial areas with the matrix [19]. Taking advantage of this characteristic, HSPM graphite can be obtained by dissolving selectively the metallic matrix. Then, surface areas and porosity can be designed during solidification process seeking to optimize shape and size of pores, electrical and thermal conductivities and flow properties.

This HSPM graphite, hereafter referred to as Aero-Eutectic Graphite (AEG), could be defined as crystalline solid with hierarchical porosity and high surface area, characterized by excellent electrical and thermal conductivities, good flow properties and low chemical reactivity. These features could be advantageous for catalysis processes, solar collectors, supporting electrode for nanofilms of Cu and electrodes for energy storage cells. Consequently, the present work reports the synthesis and characterization of AEG, and also preliminary results of its performance as a Li–O_2 battery cathode.

2. Materials and Methods

2.1. AEG Manufacturing

Gray cast iron with laminar graphite type D was used to obtain AEG by dissolving the ferrous matrix through an acid sequence. The resulting porous graphite was subsequently washed with distilled water and ethyl alcohol in order to remove the remaining acid solution. The crystalline structure was examined by X-ray diffractometer (Philips X'pert, Philips, Amsterdam, The Netherlands) with 3020 Goniometer and PW 3710 controller) using Cu Kα radiation at 35 kV and 40 mA, between 3° and 70° with a step of 0.04° and a counting time of 2 s/step. The morphological and chemical analyses of the AEG were performed using a scanning electron microscope (SEM, Carl Zeiss Ltd., Cambourne,

Cambridge, UK) with energy-dispersive X-ray spectroscopy (EDS). The determination of the surface area and porosity has been performed by Brunauer-Emmett-Teller (BET, Micromeritics ASAP 2020, Norcross, GA, USA) analysis with N_2 absorption isotherms.

2.2. Li–O_2 Battery

The electrochemical cell was a home-made Teflon body closed with standard high vacuum components. The cell ensures a uniform and fixed pressure, simple cell assembly and easy gas flow around the electrodes during the addition of oxygen.

The battery was assembled with an anode consisting of a Li metal foil (Gelon Energy Co., Vimengroad Lanshan, Rizhao, China), surface area of 0.8 cm^2 and 0.45 mm thickness), 1 M LiTFSI (lithium bis-(trifluoromethanesulfonyl)-imide, 99.95%, Sigma-Aldrich, St. Louis, MO, USA) in Triethylene glycol dimethyl ether (Triglyme) as electrolyte, a fiberglass separator (FilterLab MFV1, Filtros Anoia, S.A. Barcelona, Spain) 260 µm thickness) wetted with 0.1 mL of electrolyte and a sheet of 0.36 cm^2 and 0.7 mm thickness of AEG as a cathode. A stainless-steel disc served as a current collector. All Li–O_2 cells were assembled in an argon-filled glove box. Electrochemical measurements were carried out at 23 °C using a Bio-Logic multi-channel VMP3 potentiostat. Oxygen was forced to pass through the cell for 60 s before starting electrochemical measurements. The electrochemical test of Li–O_2 cells involves successive cycles at constant current (reduction and oxidation) with a fixed cut off in potential and capacity. During discharge, a negative current (reduction current) is applied until the potential of the cell between cathode and anode reaches 2 V or until the capacity of the cell reaches 1.2 mAh cm^{-2}. Then, charge is carried out applying a positive current (oxidation current) until the potential of the cell reaches 4.6V, or until the capacity of the cell reaches 1.2 mAh cm^{-2}. This cycle is repeated as long as it is observed that the obtained capacities are close to the set capacity value (1.2 mAh cm^{-2}).

3. Results and Discussion

3.1. AEG Characterization

In the regular practice, the cooling rates during solidification of gray cast irons are higher than those corresponding to the Fe-C equilibrium diagram. For this reason, solidification does not occur at the equilibrium temperature, but rather, at a lower temperature, producing the so-called thermal undercooling defined as:

$$\Delta T_T = T_e - T^*, \quad (1)$$

In which, T_e is the equilibrium solidification temperature and T* is the temperature of the undercooled liquid, or the temperature at which solidification occurs. At high undercooling, the ferrous phase grows dendritic, as shown in Figure 1.

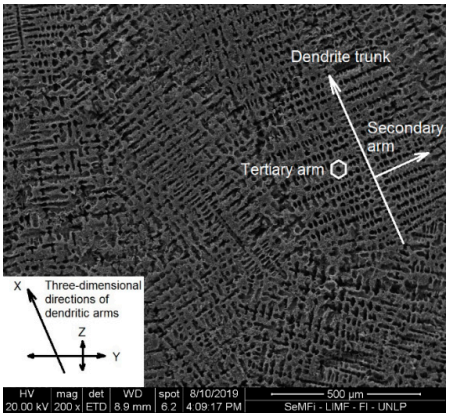

Figure 1. Dendritic structure formed by the dendrite trunk and the secondary and tertiary arms perpendicular to each other.

Dendritic structure is characterized by the growth of a main trunk in a preferred crystallographic direction, [100] in the case of ferrous materials, from which secondary and tertiary arms are developed, in a three-dimensional distribution. Under this condition of high undercooling, graphite can only grow as fine lamellae randomly distributed in the interdendritic regions of the ferrous matrix (Figure 2), which is classified by ASTM A247 standard as type D graphite.

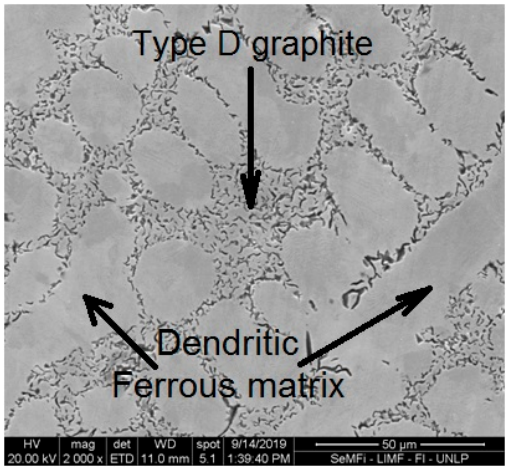

Figure 2. Gray cast iron with type D graphite.

When subjected to the acid attack sequence, the ferrous matrix is dissolved obtaining porous, and therefore, light graphite. The first step of acid dissolution sequence is performed with a non-oxidizing polyprotic acid, for which the graphite phase is immune. Fe dissolves forming a soluble complex, while other components, such as Si undergo a more complex reaction sequence which leads to the formation of an amorphous phase, mainly composed by phospho-silicates, towards the end of dissolution. Subsequently, removal of the amorphous phase is carried out by washing with a dilute solution of a strong acid that has the ability to complex such mixed compounds [19,20].

Figure 3 shows the structure of AEG formed by a continuous and interconnected network of graphite lamellae of various dimensions and randomly oriented, observing an inhomogeneous and tortuous porosity between them, with dimensions that present a wide range of nanometers to micrometers. Another characteristic observed is the quasi-cylindrical channels, perpendicular to each other in 3D distribution, originated from the dendritic structure of the ferrous matrix.

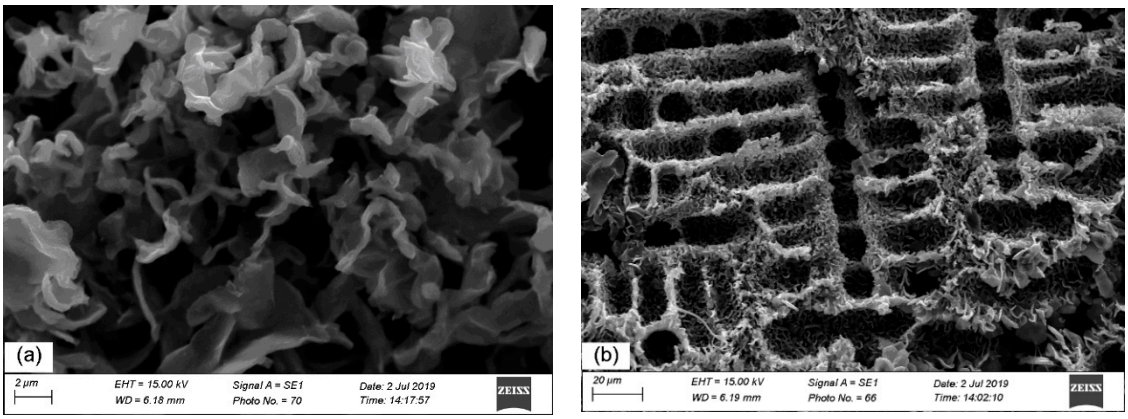

Figure 3. SEM images of AEG at different scales: (**a**) Graphite lamellae interconnected and randomly oriented; (**b**) quasi cylindrical channels formed from the dissolution of the dendritic structure of the ferrous matrix.

Surface area was characterized by BET analysis, whose results are reported in Table 1.

Table 1. Surface area of AEG measured by BET and Langmuir methods.

Property	Value
BET surface area	89.670 $m^2\ g^{-1}$
Langmuir surface area	335.978 $m^2\ g^{-1}$

Cast iron is a complex multi-component system composed of alloy elements that are present in minor proportion as Mn and Cu, and other metals that could be present as impurities as Cr, V and Ti. For that reason, chemical composition of the resulting AEG was analyzed by EDS to determine the remaining elements, which are recorded in Table 2.

Table 2. EDS analysis carried out on the AEG, in wt.%.

C	S	Cu	Fe	Si	P	Ti	V	Cr	O
95.75	0.48	1.02	0.38	0.11	0.17	0.11	0.11	0.12	1.74

Given the amount of O measured, it could be inferred that a lower amount of some elements (Fe, Si and Cr) remain as oxides, and/or carbides on the surface of the AEG. Other elements, such as Cu and Ti require particular attention, because they may intervene in the chemical reactions that develop in the batteries. It has been reported that Cu° and Cu compounds improve the oxygen reduction reaction catalytic activity in Al-air batteries [21], while Ti, as TiC, improves the redox kinetics for the catalysis of polysulfide conversion in Li-S batteries [22,23]. The presence of Cu° has a thermodynamic justification. For oxidation to occur ($M \rightarrow M^{z+} + ze^-$), the free energy variation, given by Equation (2), should be negative.

$$\Delta G^\circ = -zFE^\circ \quad (2)$$

In which, z is the number of electrons transferred; F is the Faraday's constant and E° the standard reduction potential.

According to the table of electrochemical series, Fe, Si, Mn, Cr, V that have negative reduction potential ($E^\circ < 0$) will oxidize because $\Delta G^\circ > 0$ for the reduction reaction. Cu differs from these elements because it has positive reduction potential, and therefore, it will not oxidize, being deposited on the AEG as metallic Cu nanofilms. Figure 4 shows an AEG zone with the Cu film deposited on the graphite, together with a mapping made by EDS.

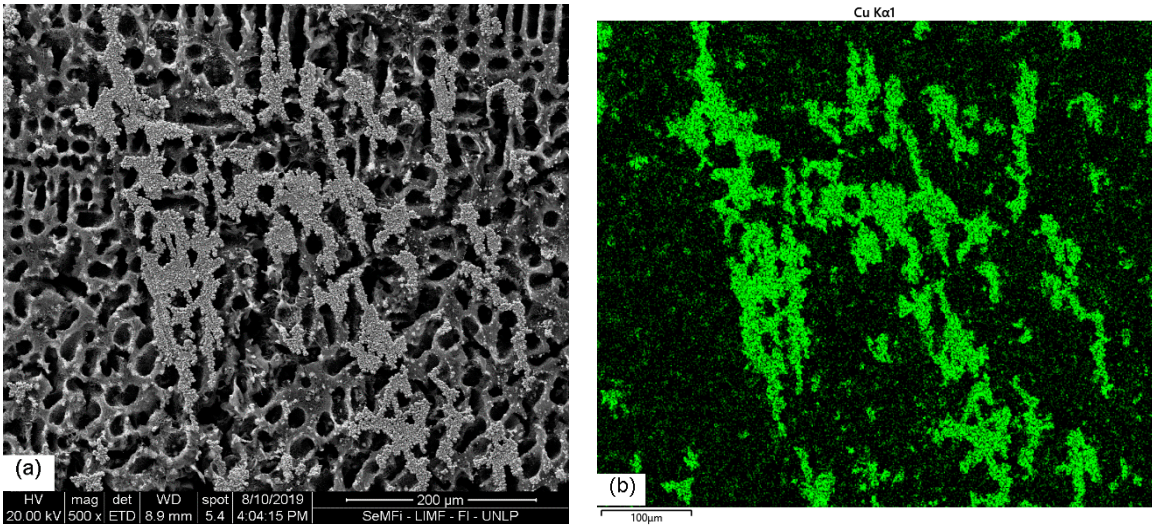

Figure 4. (**a**) SEM image of Cu nano-film deposited on the AEG; (**b**) identification of Cu by mapping carried out using EDS.

On the other hand, Ti could form small carbides during solidification of cast irons, distinguishable by their cubic appearance dispersed on the AEG, which remain unchanged during the acid attack due to their great thermodynamic stability, as shown in Figure 5. For these considerations, it may be inferred that AEG may be designed to incorporate elements that allow optimizing the functionality of the energy storage devices.

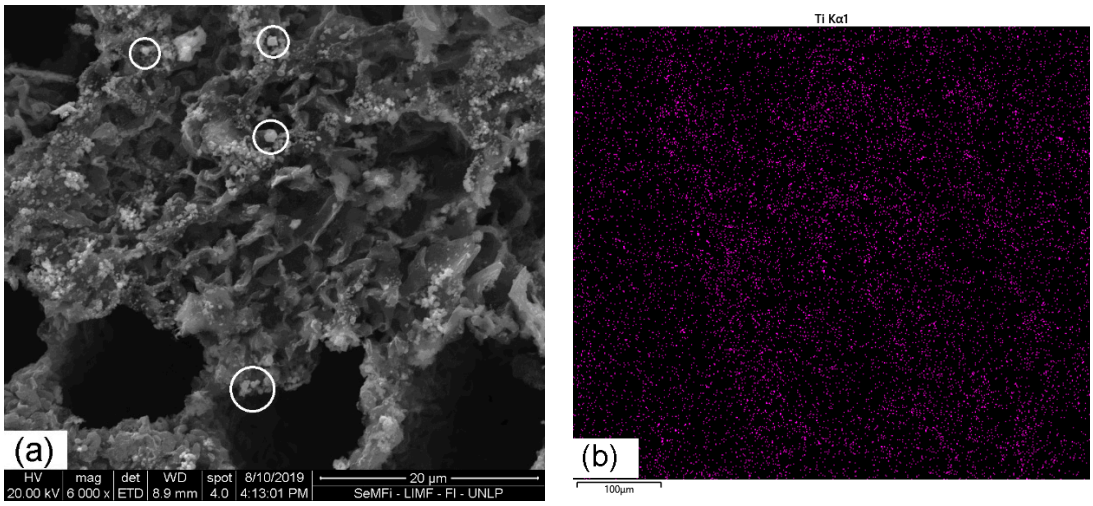

Figure 5. (**a**) Cubic TiC particles deposited on the surface of the AEG; (**b**) identification of TiC particles by EDS mapping of Ti.

X-ray diffraction technique was used to study the crystalline characteristic of AEG. The diffraction pattern of Figure 6 shows peaks at angular positions (2θ) 26.60°, 42.36°, 44.64°, 50.96° and 54.64°, which correspond to (002), (100), (101), (102) and (004) crystallographic planes of graphite, respectively.

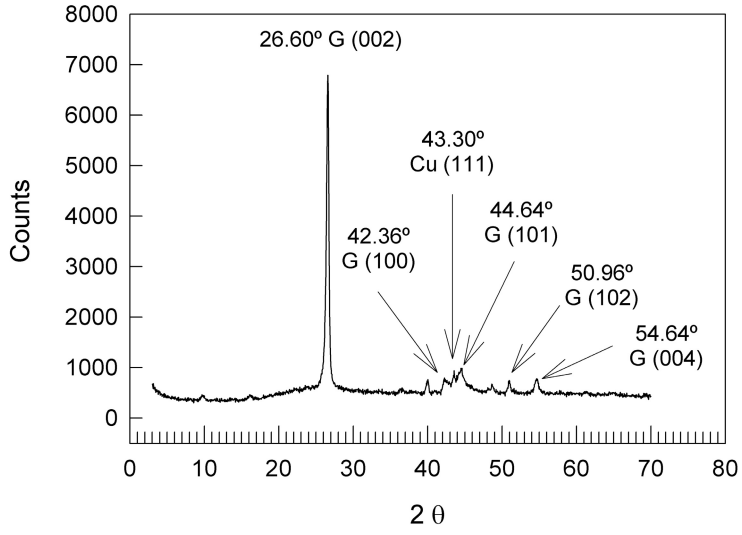

Figure 6. Crystallographic planes of AEG obtained by X-ray diffraction.

The results have been compared with those reported by Howe et al. [24] and Popova [25], who provided graphite crystallographic data, which are summarized in Table 3.

Table 3. Comparison of the angular positions of the crystallographic planes of the AEG with reported data corresponding to graphite.

HKL	2θ [H]	2θ [P]	2θ	Δ2θ [H]	Δ2θ [P]
002	26.543	26.500	**26.600**	**−0.057**	**−0.100**
100	42.360	42.400	**42.240**	**0.120**	**0.160**
101	44.555	44.600	**44.480**	**0.075**	**0.120**
102	50.689	ND	**50.960**	**−0.271**	**-**
004	54.661	54.700	**54.640**	**0.021**	**0.060**

[H] Howe et al. data; [P] Popova data; Δθ difference in the angular position; in bold, data of present paper.

There is a good agreement in the 2θ angular positions, although it has been noticed greater shift in the (102) peak at 2θ = 50.960°, according to the data reported by Howe regarding this reflection. In this case, it is possible that the reflection does not correspond to (102) hexagonal graphite, but to {10.1} of rhombohedral phase of graphite, as reported by Roviglione and Hermida in their work on nodular graphite [20]. However, this allotropic variety, which is formed out of tensions undergone in the hexagonal graphite, will be shown in a minor proportion and according to the recorded intensity of the peak. The diffraction pattern also shows a small peak at 2θ = 43.300°, which considering the amount of Cu detected by EDS, may be ascribed to the (111) peak of this element.

3.2. AEG as Cathode in Li–O_2 Battery

The operation of Li–O_2 batteries is characterized by the oxygen reduction reaction (ORR) and the oxygen evolution reaction (OER) that occur during the charge and discharge processes. These heterogeneous reactions involve three phases: the oxygen dissolved in the electrolyte, the Li^+ ion and the cathode (solid electrode). Consequently, the pore network is of great importance, because the contact between the phases is one of the key factors to improve the efficiency and cyclability of the batteries, in addition to the fact that an adequate network of open macropores would facilitate ionic transport [26,27]. The relationship between electrical performance and pore morphology is given by the fact that lithium peroxide is insoluble in non-aqueous solvents and precipitates on the internal surface of the cathode pores and, as it is not a good ionic-electronic conductor, it passivates the surface of the pores and can occlude them [28,29]. A suitable porous cathode is therefore required to accommodate the discharge product (Li_2O_2) and facilitate diffusion of oxygen gas to the reaction site through the pore structure and the lithium peroxide film. The porous cathode must also provide sufficient conductivity for electrons to reach the reaction site efficiently without increasing the ohmic impedance of the electrode.

As proof of concept, AEG has been tested in Li–O_2 batteries as it has been synthesized, without the addition of binders, or any extra conductive carbon. The absence of binder avoids the possible problems that may arise from its use, such as decomposition that would decrease battery performance.

A cyclic voltammetry test has been first conducted in order to evaluate its performance as a cathode. Figure 7 shows that position and shape of the peaks are similar to those reported in previous works on Li–O_2 cells containing similar electrolyte [30,31]. According to these results, it may be inferred that the contact between the electrolyte and AEG acting as a cathode is satisfactory enough to produce the oxygen reduction reaction (ORR, starting near 2.6 V), and the reaction of evolution of oxygen (OER, starting about 3.2 V).

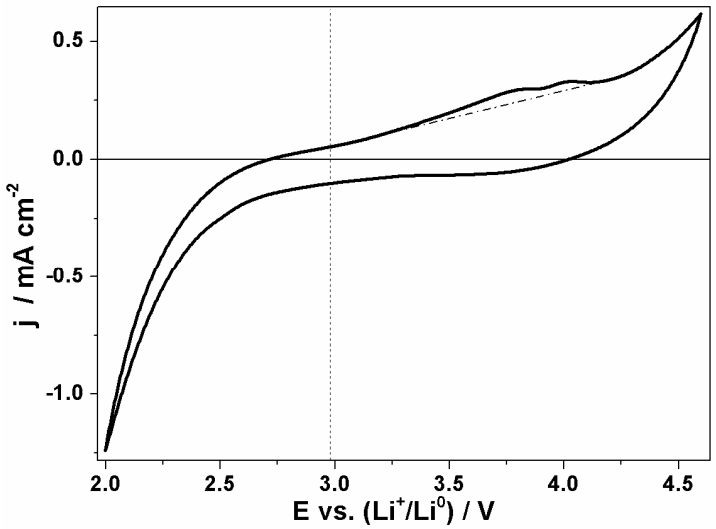

Figure 7. Cyclic voltammetry at 0.02 V s^{-1} for 1 M LiTFSI in triethylene glycol dimethyl ether (Triglyme) electrolyte in an oxygenated cell. Oxidation peaks are highlighted with a baseline in gray. Vertical dark dotted line: theoretical working potential of Li–O_2 battery, 2.96 V.

During the OER, two oxidation peaks can be seen. There are some discrepancies on their origin. Some authors attribute them to the formation of lithium superoxide and lithium peroxide, respectively [31], while others mention the formation of particles of different sizes, or thicknesses of the lithium peroxide layer [32]. The peaks could also be attributed to the formation of different structures of lithium peroxide, either in the crystalline or amorphous phase [33]. Among these, the amorphous phase is preferred, because it presents higher electrical conductivity, which is beneficial for the greater efficiency of the battery.

As a demonstration of the suitability of AEG as cathode material in Li–O_2 batteries, galvanostatic charge-discharge tests were performed at a typical current density of 0.1 mA cm^{-2}, working at a discharge capacity of 1.2 mAh cm^{-2}. The potential vs. capacity curves of Figure 8 shows that the battery accomplishes twenty complete cycles, keeping the capacity value fixed. The results were similar to those of previous reports using the same electrolyte [5,34]. Notice that the twenty limited discharge-charge cycles at 1.2 mAh cm^{-2} gives an accumulated capacity of 24 mAh cm^{-2}, which is equivalent to conventional 48 cycles limited to 0.5 mAh cm^{-2}. Regarding to that, the reported value in this work is in the range of values reported that could be found in the vast literature of batteries: Pd/Carbon Nano Fibers hybrid material with different dopamine hydrochloride concentrations in the synthesis achieves 21, 33 and 49 cycles limited to 0.2 mAh cm^{-2} (current density 0.1 mA cm^{-2}) [35]. Commercial carbon paper (SGL group, BC35) cathode reaches 10, 15 and 60 cycles limited to 0.52 mAh cm^{-2} without catalyzer, and with LiBr and $RuBr_3$ catalyzers, respectively (current density 0.1 mA cm^{-2}) [36]. The battery with carbonized polyacrylonitrile cathode using BBQ and TEMPO as mediators and 20,000 ppm of added water reaches 20 cycles limited to 1 mAh cm^{-2} (current density 0.5 mA cm^{-2}) [37].

Probably, the charge potential used may have increased beyond 4.6 V, as reported in some previous works [35,38,39], assuming that the actual potential on the interface never reaches this value, and that the effect is attributed to an ohmic potential that increases it.

The observed capacity fade on the charge could be ascribed to the increased reaction potential beyond 4.6 V and the impossibility to remove all the ORR products deposited on the electrode surface, passivating it.

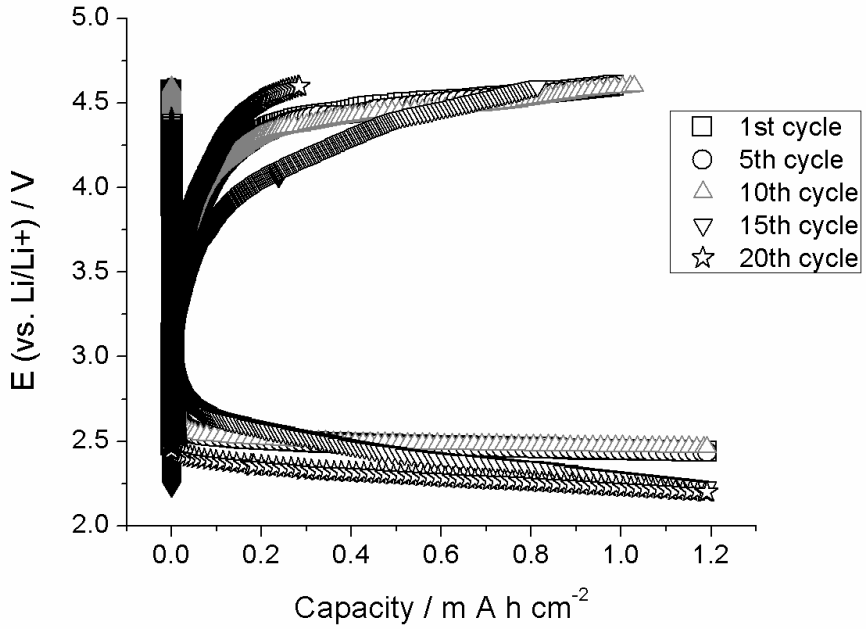

Figure 8. Voltage (vs. Li^+/Li^0) as a function of capacity (mAh cm^{-2}) for AEG cathode in 1 M LiTFSI in triglyme (oxygenated solution) at a current density of 0.1 mA cm^{-2}. Discharge limited to 1.2 mAh cm^{-2}.

4. Conclusions

AEG can be defined as a lightweight and hierarchically porous material that is obtained from the solidification of low-cost materials, such as gray cast irons.

Dissolving the ferrous matrix of those materials by means of the use of an acid sequence gives crystalline graphite with high porosity and a relatively high surface area.

In the present work, AEG has been obtained from type D gray cast iron, having interlamellar slits of inhomogeneous porosity, which range from nanometers to micrometers and quasi-cylindrical channels in a three-dimensional arrangement. Preliminary results of its use as cathode in Li–O_2 batteries have been promising. Cyclic voltammetry tests have shown that contact with the electrolyte is satisfactory enough for the ORR and OER reactions to develop. While in the discharge-charge-galvanostatic tests the battery accomplishes 20 complete cycles limited at 1.2 mAh cm^{-2}.

An important concept to consider is the feasibility of improving the properties of AEG through functionalization procedures that optimize its performance, or adapt it to different specific requirements, such as the deposition of metallic Cu nanofilm or TiC.

Author Contributions: Conceptualization, A.N.R.; methodology, A.N.R. and R.W.G.; validation A.Y.T. and J.L.G.-C.; investigation, A.N.R. and R.W.G.; data curation, A.Y.T.; writing—original draft preparation, A.N.R., R.W.G. and A.Y.T.; writing—review and editing, J.L.G.-C.; funding acquisition R.W.G. All authors have read and agreed to the published version of the manuscript.

Funding: This research received no external funding.

Acknowledgments: The authors also give special thanks to the Comisión de Investigaciones Científicas de la Provincia de Buenos Aires (CICPBA), Centro de Investigación y Desarrollo en Materiales Avanzados y Almacenamiento de Energía de Jujuy (CIDMEJu) and Facultad de Ingeniería de la Universidad de Buenos Aires (FIUBA) for their financial support to carry out the experimental works.

Conflicts of Interest: The authors declare no conflict of interest.

References

1. Razzaq, L.; Farooq, M.; Mujtaba, M.; Sher, F.; Farhan, M.; Hassan, M.T.; Soudagar, M.E.M.; Atabani, A.; Kalam, M.; Imran, M. Modeling viscosity and density of ethanol-diesel-biodiesel ternary blends for sustainable environment. *Sustainability* **2020**, *12*, 5186. [CrossRef]
2. Yang, Z.; Zhang, J.; Kintner-Meyer, M.C.W.; Lu, X.; Choi, D.; Lemmon, J.P.; Liu, J. Electrochemical energy storage for green grid. *Chem. Rev.* **2011**, *111*, 3577–3613. [CrossRef]
3. Arunachalam, V.; Fleischer, E. The global energy landscape and materials innovation. *MRS Bull.* **2008**, *33*, 264–276. [CrossRef]
4. Dutta, S.; Bhaumik, A.; Wu, K.C.-W. Hierarchically porous carbon derived from polymers and biomass: Effect of interconnected pores on energy applications. *Energy Environ. Sci.* **2014**, *7*, 3574–3592. [CrossRef]
5. Xu, W.; Hu, J.Z.; Engelhard, M.H.; Towne, S.A.; Hardy, J.; Xiao, J.; Feng, J.; Hu, M.Y.; Zhang, J.; Ding, F.; et al. The stability of organic solvents and carbon electrode in nonaqueous Li-O2 batteries. *J. Power Source* **2012**, *215*, 240–247. [CrossRef]
6. Su, B.L.; Sánchez, C.; Yang, X.-Y. *Hierarchically Structured Porous Materials: From Nanoscience to Catalysis, Separation, Optics, Energy, and Life Science*, 1st ed.; Wiley VCH: Weinheim, Germany, 2012.
7. Li, Y.; Fu, Z.Y.; Su, B.L. Hierarchically structured porous materials for energy conversion storage. *Adv. Funct. Mater.* **2012**, *22*, 4634–4667. [CrossRef]
8. Sun, M.H.; Huang, S.Z.; Chen, L.H.; Li, Y.; Yang, X.Y.; Yuan, Z.Y.; Su, B.L. Application of hierarchically structured porous materials from energy storage and conversion, catalysis, photocatalysis, adsorption, separation and sensing to biomedicine. *Chem. Soc. Rev.* **2016**, *45*, 3479–3563. [CrossRef]
9. Yang, X.Y.; Chen, L.H.; Li, Y.; Rooke, J.C.; Sanchez, C.; Su, B.L. Hierarchically porous materials: Syntesis strategies and structure design. *Chem. Soc. Rev.* **2017**, *46*, 481–558. [CrossRef]
10. Thompson, B.R.; Horozov, T.S.; Stoyanov, D.D.; Paulov, V.N. Hierarchically structured composites and porous materials from soft templates: Fabrication and applications. *J. Mater. Chem.* **2019**, *A7*, 8031–8049. [CrossRef]
11. Wang, H.; Chen, H.; Wang, H.; Wu, L.; Wu, Q.; Luo, Z.; Wang, F. Hierarchical porous FeCo2O4@Ni as a carbon and binder-free cathode for lithium−oxygen batteries. *J. Alloy. Comp.* **2019**, *780*, 107–115. [CrossRef]
12. Gang, Y.; Wei, Z.; Wang, J.; Zhang PLi, H.; Wang, Y. Design and fabrication of hierarchically porous carbon with a template-free method. *Sci. Rep.* **2014**, *4*, 6349. [CrossRef]
13. Liu, B.; Shioyama, H.; Akita, T.; Xu, Q. Metal-organic framework as a template for porous carbon synthesis. *J. Am. Chem. Soc.* **2008**, *130*, 5390–5391. [CrossRef]
14. Sakintuna, B.; Actaş, Z.; Yürüm, Y. Synthesis of porous carbon materials by carbonization in natural zeolite nanochannels. *Prepr. Pap.-Am. Chem. Soc. Div. Fuel Chem.* **2003**, *48*, 614–615.
15. Craig, D.B.; Hornung, M.J.; McCluhan, T.K. Gray iron. In *ASM Handbook "Casting"*, 9th ed.; Davis, J.R., Ed.; ASM International: Cleveland, OH, USA, 1998; Volume 15, pp. 1365–1404.
16. Riposan, I.; Chisamera, M.; Stan, S.; White, D. Complex (Mn, X)S compounds—Major sites for graphite nucleation in grey cast iron. *China Foundry* **2009**, *6*, 352–357.
17. Marsh, H.; Rodríguez-Reinoso, F. Production and reference material. *Act. Carbon* **2006**, 454–508. [CrossRef]
18. *ASTM A247-19, Standard Test Method for Evaluating the Microstructure of Graphite in Iron Castings*; ASTM International: West Conshohocken, PA, USA, 2019. [CrossRef]
19. Roviglione, A.N.; Gregorutti, R.W.; Kempf, R.A. Ultra-light porous materials tailored from solidification and solid state processes. *Mater. Methods Technol.* **2015**, *9*, 169–177.
20. Roviglione, A.N.; Hermida, J.D. Rhombohedral graphite phase in nodules from ductile cast iron. *Proc. Mater. Sci.* **2015**, *8*, 924–933. [CrossRef]
21. Li, F.; Li, J.; Feng, Q.; Yan, J.; Tang, Y.; Wang, H. Significantly enhanced oxygen reduction activity of Cu/CuNxCy co-decorated ketjenblack atalyst for Al-air batteries. *J. Energy Chem.* **2018**, *27*, 419–425. [CrossRef]
22. Tang, X.; Xu, Z.; Sun, Z.; Zhou, J.; Wu, X.; Lin, H.; Rong, J.; Zhuo, S.; Li, F. Factors of kinetics processes in lithium-sulfur reactions. *Energy Technol.* **2019**, *7*, 1900574. [CrossRef]
23. Peng, H.J.; Zhang, G.; Chen, X.; Zhang, Z.-W.; Xu, W.-T.; Huang, J.-Q.; Zhang, Q. Frontispiece: Enhance electrochemical kinetics on conductive polar mediators for lithium-sulfur batteries. *Angew. Chem. Int. Ed. Engl.* **2016**, *55*, 12990–12995. [CrossRef]

24. Howe, J.Y.; Rawn, C.J.; Jones, L.E.; Ow, H. Improved crystallographic data for graphite. *Powder Diffr.* **2003**, *18*, 150–154. [CrossRef]
25. Popova, A.N. Crystallographic analysis of graphite by X-ray diffraction. *Coke Chem.* **2017**, *60*, 361–365. [CrossRef]
26. Yuan, J.; Yu, J.-S.; Sundén, B. Review on mechanisms and continuum models of multi-phase transport phenomena in porous structures of non-aqueous Li-Air batteries. *J. Power Sources* **2015**, *278*, 352–369. [CrossRef]
27. Lim, H.-D.; Yun, Y.S.; Ko, Y.; Bae, Y.; Song, M.Y.; Yoon, H.J.; Kang, K.; Jin, H.-J. Three-dimensionally branched carbon nanowebs as air-cathode for redox-mediated Li-O2 batteries. *Carbon* **2017**, *118*, 114–119. [CrossRef]
28. Christensen, J.; Albertus, P.; Sanchez-Carrera, R.S.; Lohmann, T.; Kozinsky, B.; Liedtke, R.; Ahmed, J.; Kojic, A. A critical review of Li/air batteries. *J. Electrochem. Soc.* **2012**, *159*, R1–R30. [CrossRef]
29. Viswanathan, V.; Thygesen, K.S.; Hummelshoj, J.S.; Norskov, J.K.; Girishkumar, G.; McCloskey, B.D.; Luntz, A.C. Electrical conductivity in Li2O2 and its role in determining capacity limitations in non-aqueous Li-O2 batteries. *J. Chem. Phys.* **2011**, *135*, 214704. [CrossRef]
30. Ferrari, S.; Quartarone, E.; Tomasi, C.; Bini, M.; Galinetto, P.; Fagnoni, M.; Mustarelli, P. Investigation of ether-based ionic liquid electrolytes for Lithium-O2 batteries. *J. Electrochem. Soc.* **2015**, *162*, A3001–A3006. [CrossRef]
31. Laoire, C.O.; Mukerjee, S.; Abraham, K.M.; Plichta, E.J.; Hendrickson, M.A. Influence of nonaqueous solvents on the electrochemistry of oxygen in the rechargeable lithium-air battery. *J. Phys. Chem.* **2010**, *C 114*, 9178–9186. [CrossRef]
32. Guo, L.; Wang, J.; Ma, S.; Zhang, Y.; Wang, E.; Peng, Z. The origin of potential rise during charging of Li-O2 batteries. *Sci. China Chem.* **2017**, *60*, 1527–1532. [CrossRef]
33. Cui, Q.; Zhang, Y.; Ma, S.; Peng, Z. Li2O2 oxidation: The charging reaction in the aprotic Li-O2 batteries. *Sci. Bull.* **2015**, *60*, 1227–1234. [CrossRef]
34. Lai, J.; Xing, Y.; Chen, N.; Li, L.; Wu, F.; Chen, R. A comprehensive insight into the electrolytes for rechargeable lithium–air batteries. *Angew. Chem.* **2019**. [CrossRef]
35. Tamakloe, W.; Agyeman, D.A.; Park, M.; Yang, J.; Kang, Y. Polydopamine-induced surface functionalization of carbon nanofiber for Pd deposition enabling an enhanced catalytic activity for oxygen reduction and evolution reactions. *J. Mater. Chem. A* **2019**, *7*, 7396–7405. [CrossRef]
36. Lee, S.H.; Kwak, W.-J.; Sun, Y.-K. A new perspective of the ruthenium ion: Bifunctional soluble catalyst for high efficiency Li-O2 batteries. *J. Mater. Chem. A* **2017**, *5*, 15512–15516. [CrossRef]
37. Liu, T.; Frith, J.T.; Kim, G.; Kerber, R.N.; Dubouis, N.; Shao, Y.; Liu, Z.; Magusin, P.C.M.M.; Casford, M.T.L.; Garcia-Araez, N.; et al. The Effect of Water on Quinone Redox Mediators in Nonaqueous Li-O2 Batteries. *J. Am. Chem. Soc.* **2018**, *140*, 1428–1437. [CrossRef]
38. Lv, Y.; Li, Z.; Yu, Y.; Yin, J.; Song, K.; Yang, B.; Yuan, L.; Hu, X. Copper/cobalt-doped LaMnO3 perovskite oxide as a bifunctional catalyst for rechargeable Li-O2 batteries. *J. Alloy. Comp.* **2019**, *801*, 19–26. [CrossRef]
39. Zheng, C.; Ding, W.; Wang, C. N-methyl-N-propyl Pyrrolidine Bromide (MPPBr) as a bifunctional redox mediator for rechargeable Li-O2 batteries. *J. Mater. Chem. A* **2019**, *7*, 6180–6186. [CrossRef]